Electronic Supplementary Information

for

"UV Wavelength-Dependent Photoionization Quantum Yields for the Dark $^1n\pi^*$ State of Aqueous Thymidine"

Piao Xu,[a,b] Dongdong Wang, [a,b] Duoduo Li, [a,b] Jinyou Long, *[a,b] Song Zhang, *[a,b] Bing Zhang[a]

Content:

S1. Experimental method

The experimental apparatus utilized in this work consists of a commercial femtosecond laser system and a liquid-microjet magnetic-bottle photoelectron spectrometer. Briefly, a Ti:sapphire regenerative amplifier system (Coherent Mira-Legend) output the fundamental wavelength of 800 nm with a repetition rate of 1 kHz and a pulse duration of 100 fs. The total output energy of 4mJ/pulse was split into three parts, one of which was used to pump an optical parametric amplifiers (OPA) (Light Conversion, TOPAS-C) to directly output the experimental UV wavelengths ranging from 240 to 267 nm. The experimental energies for the UV pulses were attenuated to be on the order of several or hundreds of nJ/pulse to avoid gas-phase signals. The UV pulse was softly focused on the liquid microjet with a spherical plano-convex len (f=300 mm).

The liquid-microjet magnetic-bottle photoelectron spectrometer consists of a liquid-microjet injection system and a magnetic-bottle photoelectron spectrometer. The liquid-microjet injection system was similar to that of our liquid-microjet photoelectron imaging spectrometer[1]. Briefly, a home-made liquid microjet nozzle consisted of a fused silica capillary with a length of 8 mm and an inner diameter (I.D.) of 25 μm. Note that the conductive graphite was carefully coated to the outer surface of the nozzle to improve the silica's electrical conductivity. The nozzle assembly was then installed to a three-axis xyz translation stage with a minimum adjustable precision of 1 μm. As a result, the microjet was injected into the source chamber from the top to the bottom direction through the nozzle under an accurate flow control by a high-pressure liquid chromatography (HPLC) pump. Under a typical jet flow rate of 0.5 mL/min, the microjet consists of a smooth laminar flow for 2 to 3 mm downstream from the orifice. And then the microjet enters the turbulent flow regime and breaks into droplets. The microjet is finally collected and frozen out by a liquid nitrogen cold trap, which is located about 120 mm downstream from the orifice. A semi-automatic refill system was developed to deliver liquid nitrogen from a pressurized liquid nitrogen tank into the liquid nitrogen cold trap through thermally insulated copper pipes.

The magnetic-bottle photoelectron spectrometer was also previously described[2]. Briefly, the magnetic-bottle system was realized by a combination of a strong permanent magnetic field (SmCo magnet, ~0.98T at its tip) located inside the source chamber and a weak union magnetic field (solenoid coils, 10G) located inside the TOF chamber. The source chamber was used to produce the liquid microjet. The TOF chamber was used to guide the photoelectrons to the electron detector. The source and TOF chambers shield the stray magnetic field through the double-layer μ-metal tube. A Polyetheretherketone (PEEK) tube with an inner diameter of 100 μm without capillary is used at the gas nozzle exit to introduce the gasous nitric oxide (NO) to perform a dialy calibration of the spectrometer.

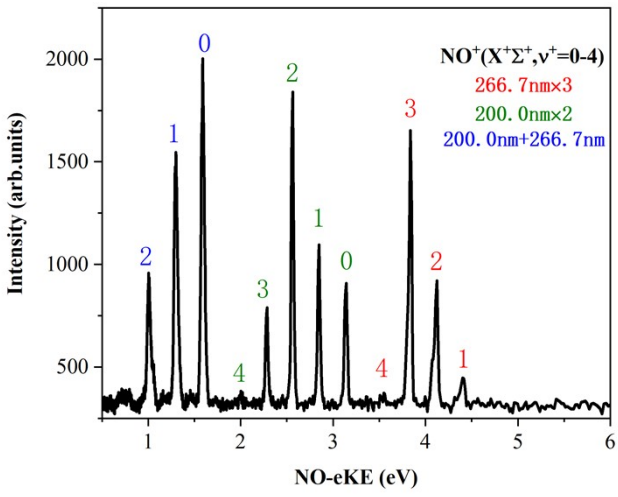

Fig. S1. Electron kinetic energy spectrum calibrated by nonresonant multiphoton ionization signals of NO at 200 nm, 266.7 nm and at their time zero.

The photoelectron kinetic energy (PKE) or electron kinetic energy (eKE) spectra measured in the experiment were calibrated based on the NO ionization spectra measured by Jarvis[3] and Buchner[4], and the relationship between flight of time of photoelectrons and their PKE was obtained by the following equation：

$$E_k = 2.8428 \times 10^6 \times \left(\frac{S_0}{t - T_0}\right)^2 - E_0 \qquad (1)$$

Among them, S_0 represents the electron flight distance, T_0 represents the time difference between the time of data collection and the time of electron ionization, and E_0 represents the combined offset value of the PKE that results from the spectrometer. The fitted parameters are S_0=1.134 m, T_0=35.99 ns, E_0=-0.16534 eV. The S_0 is in good agreement with the flight tube length of 1.16 m designed for the experimental setup. The total TOF length was designed to be 1.16 m, allowing for a photoelectron kinetic energy resolution approximately equal to 50 meV below 10 eV when a femtosecond pulse was used, as shown in Fig. S1. Moreover, an analysis of the time-resolved non-resonant multiphoton ionization signal of gaseous NO determined that the cross-correlation (or instrument response function (IRF)) between two pulses was approximately 257 fs and an estimated of the UV pulse duration was approximately 180 fs.

Thymidine (Thd) (≥99% purity) used in the experiments were purchased from the commercial company (Aladdin) without further purifications. The sample solutions of Thd (100 mM, 10 μM) were prepared using ultrapure water (18.2 MΩ·cm) at room temperature. In addition, 30 mM sodium fluoride (NaF, ≥99%, Aladdin) was added to minimize the streaming potential of the aqueous microjet[5]. The 100 mM aqueous Thd was used for the photoionization experiments (pH=5.2), as discussed below, the 10 μM aqueous Thd was used for the UV absorption measurement. In our spectroscopic experiments reported in Figure 3, the PH of the aqueous thymidine solution was approximately 5.2. Note that the acidity or alkalinity of solvents could impact the charge distribution and transition rates of excited-state molecules by altering their charge states through protonation or deprotonation processes[6]. However, we didn't consider this influence in our work. In this work, a 25 μm internal diameter (I.D.) capillary was used as the microjet orifice and the flow rate was controlled to be 0.5 mL/min by a HPLC pump (PU-4180, JASCO)[5]. Under the working conditions described above, the vacuum in the source chamber was maintained at around 1-3×10^{-2} Pa, whilst the vacuum in the TOF detection chamber was maintained at around 2-3×10^{-4} Pa.

The electron binding energy (eBE) of the molecular orbital from which the electron is ionized, with respect to the electronic state of the cation that is left behind, can be found using the formula eBE = 3hν - PKE, where 3hν is the photon energy. This can be done by measuring the PKE distribution of photoelectrons emitted after photoionization (see Fig. S2).

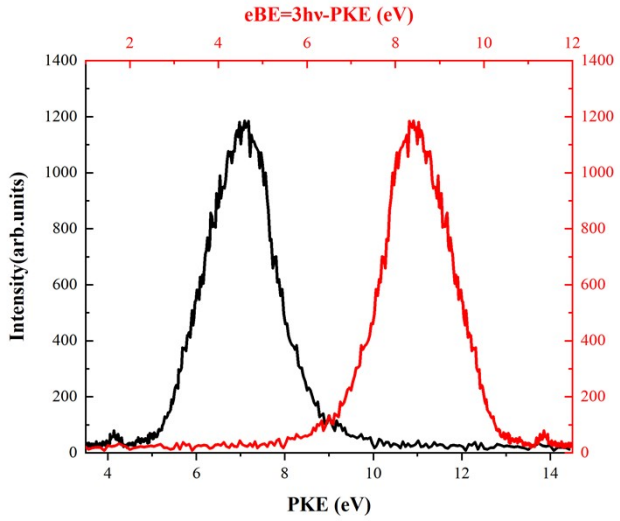

Fig. S2. Conversion between PKE (black) and eBE (red) obtained by photoionization of thymidine in aqueous solution at 240.0 nm

S2. Steady-state absorption spectra

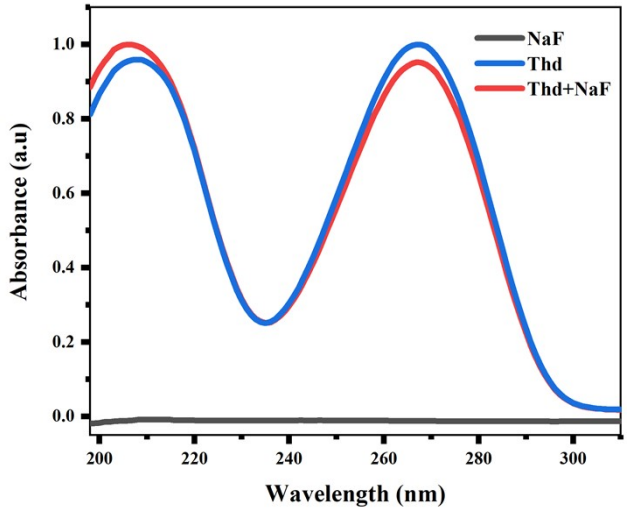

Fig. S3. Comparison of steady-state absorption spectra of 30 mM NaF aqueous solution (shown in black line), 10 μM aqueous Thd (shown in blue line), 10 μM Thd+30 mM NaF aqueous solution (shown in red line) under UV irradiation.

As discussed above, 30 mM sodium fluoride (NaF, ≥99%) was added to minimize the streaming potential of the aqueous microjet. To evaluate the influence of the addition of NaF, the steady-state absorption spectra of 30 mM NaF aqueous solution (shown in black line), 10 μM aqueous Thd (shown in blue line), 10 μM Thd+30 mM NaF aqueous solution (shown in red line) were shown in Fig. S3. Note that the 10 μM aqueous Thd was chosen to avoid absorption saturation. The 100 mM aqueous Thd was used for the photoionization experiments, similar to the concentration of 150 mM aqueous Thd in a phosphate buffer used by Suzuki and co-workers[7]. We did not use a phosphate buffer to enhance its solubility. As shown in Figure S3, small band shifts are observed for the second absorption bands centered at about 208 nm, while the first absorption bands centered at about 266 nm exhibit no obvious band shift between 240 nm and 300 nm and the only small changes are their relative band intensities. These changes seemingly suggest that NaF could more or less affect the electronic structure of thymidine. The small pH change induced by the addition of NaF is considered within an acceptable range for our experiments, as evidenced by the pH 5.2 of the aqueous thymidine solution. Notably, the addition of 30 mM NaF does not result in any photoionization signals out of the F^- and Na^+. In this kind of liquid microjet photoelectron spectroscopy, whether the addition of the halide salts may affect the electronic structure (i.e., energies, energy order, multiphoton absorption or ionization cross sections of the excited states) of thymidine and its excited state dynamics is currently unknown. Our steady-state absorption experiments seemingly indicate that the addition of NaF does not significantly affect the UV absorption of aqueous thymidine under UV irradiation ranging from 240.0 nm to 266.7 nm.

Moreover, thymidine-thymidine cyclobutane photodimers and other photoproducts at high concentrations should be worthy of notice. The paper[8] is a pioneering work to demonstrate the formation of photodamage product of cyclobutane pyrimidine dimer in a single-stranded $(dT)_{18}$. In our experiment, we used a 100 mM concentration, which is somewhat lower than that recently used by Prof. Suzuki's group of 150 mM[7]. We chose the 100 mM concentration in order to both maximize the photoelectron signals and might minimize the formation of the thymidine dimerization. Because Prof. Suzuki's group reported that they also performed experiments using 15 mM thymidine and suggested that the lifetimes and quantum yield for thymidine are not strongly influenced by any aggregation of thymidine nucleobases[6]. Therefore, we didn't consider the formation of photoproducts such as dimers in our previous manuscript. In order to assess whether thymidine undergoes photodegradation upon excitation by a comparation of the steady-state absorption spectra of the samples with and without the irradiated UV laser pulses. We have measured the steady-state absorption spectra of the aqueous thymidine solutions with and without the irradiated UV laser pulses at two wavelengths of 240.0 nm and 266.7 nm. The comparative steady-state absorption spectra are shown in Fig S4. For the first absorption bands centered at about 266 nm (marked by the red vertical dotted line), there is no obvious band shift between 240 nm and 280 nm and the only subtle changes are their relative band intensities (The relative absorbance values were 1.000, 0.967, and 0.994, and thus a subtle change in intensity is less than 4%). In particular, the absorption spectra with and without the irradiated pulse at 240.0 nm show that their first absorption band are exactly the same. On the other hand, small band shifts are observed for the second absorption bands centered at about 208 nm (marked by

the blue vertical dotted line) when the aqueous thymidine solutions are irradiated by the UV laser pulses at 240.0 nm and 266.7 nm. A comparation of the features of the first and second absorption bands of the aqueous thymidine solutions with and without the irradiated UV laser pulses seems to suggest that there is a negligible influence on the first absorption bands by the thymidine dimerization and its photodegradation. Because there is nearly no band shift for the first absorption bands. As expected, the photoexcitation and photoionization processes are likely to prefer to occur on the thymidine monomer unit even when thymidine dimers are present. Morevore, according to femtosecond time-resolved infrared experiments on thymine single strands, cyclobutane thymine dimers are fully formed in ~1 picosecond after ultraviolet excitation[8]. More importantly, it should be noted that the concentration for the thymidine monomer is usually at least an order of magnitude larger than that for the thymidine dimers in the aqueous thymidine solution of high concentration. These above aspects might also explain why Prof. Suzuki's group claimed that the lifetimes and quantum yield for thymidine are not strongly influenced by any aggregation of thymidine nucleobases[7]. Therefore, we speculate that the thymidine photodegradation might not occur during our photoexcitation and photoionization processes within a time window of ~ 180 fs.

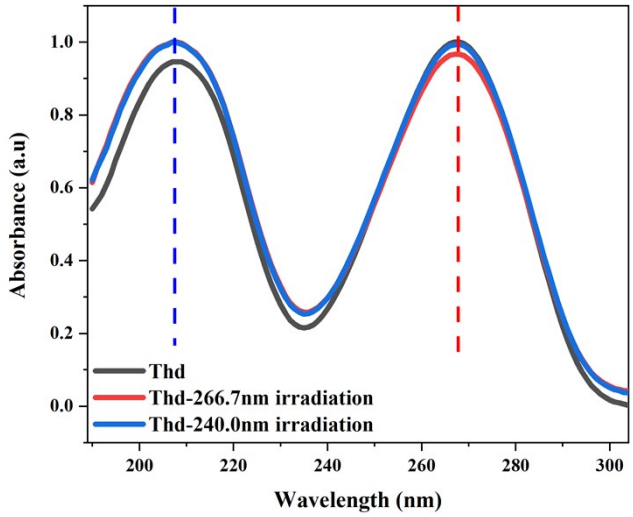

Fig. S4. A comparative steady-state absorption spectra of aqueous thymidine solutions with and without irradiation at 240.0nm and 266.7nm. The first absorption bands centered at about 266 nm (marked by the red vertical dotted line), there is no obvious band shift between 240 nm and 280 nm and the only subtle changes are their relative band intensities (The relative absorbance values were 1.000, 0.967, and 0.994, and thus a subtle change in intensity is less than 4%). Small band shifts are observed for the second absorption bands centered at about 208 nm (marked by the blue vertical dotted line) when the aqueous thymidine solutions are irradiated by the UV laser pulses at 240.0 nm and 266.7 nm.

S3. Laser power dependence

To distinguish between the two- and three-photon ionization schemes, we further examine the laser power dependence of the ionizing liquid water $^1b_1$ signal. Other unidentified stronger signals severely overlap with the two ionization channels ($^1\pi\pi^* \rightarrow D_0$ (π^{-1}) and $^1n\pi^* \rightarrow D_1$ (n^{-1})) when the laser energy increases to more than 1000 nJ (not shown here), resulting in big uncertainty to extract the two ionization channel components. However, the $^1b_1$ signal shows no interrupt. Especially, the $^1b_1$ signal is easier to appear at 246.33 nm. Thus, we used the $^1b_1$ signal following the photoionization at 246.33 nm to perform the laser power dependence.

Multiphoton absorption cross-section:

$$\delta = \delta_0 (\frac{I}{I_s})^n \qquad (2)$$

δ: Multiphoton absorption cross-section, δ_0: basic absorption cross-section, I: light intensity, I_s: saturated light intensity, n: number of photons

For Gaussian pulsed lasers, the relationship between the light intensity and the single pulse energy of the pulsed laser can be expressed by the following formula:

$$I = \frac{E}{\pi r^{2\tau}} \qquad (3)$$

I: light intensity, E: single pulse energy, r: spot radius, τ: pulse duration.

By taking the logarithm and simplifying it, the following formula is obtained:

$$lg\delta = A + nlgE \qquad (4)$$

Where A is a constant.

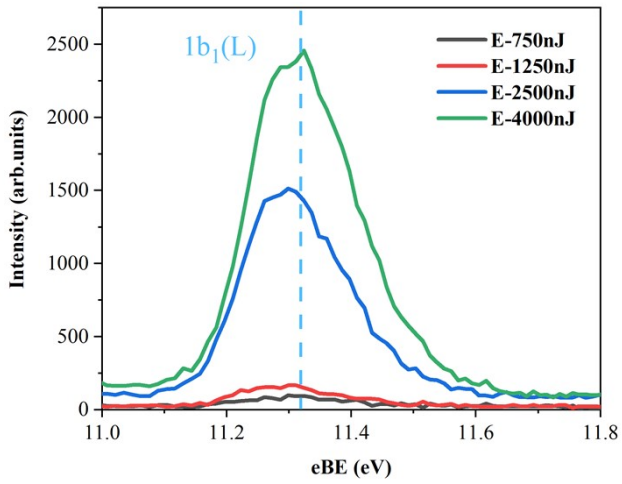

Fig. S5. Three-photon ionization electron binding energy (eBE) spectra of the liquid water $^1b_1$ at 246.33 nm for. The E in the figure represents the single pulse energy and the abscissa represents the converted eBE with a dashed value of 11.33eV[9].

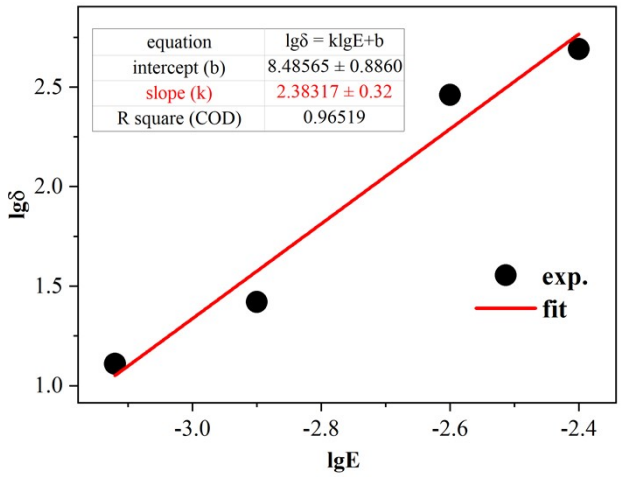

Fig. S6. The laser power dependence obtained from Fig. S5. The slope of the straight line is ~2.4, indicative of a preferred three-photon ionization scheme.

In our experiment, we can observe the ionization signal of liquid water ^{1b_1} by changing the laser energy of the UV pulse, ionizing signals of liquid water ^{1b_1}with different intensities can be obtained, as shown in Fig. S5. The value

of $1b_1$ in liquid water was used to correct all the eBE spectra based on the most recent accurate measurement by Thürmer et al[9]. The UV radiation employed in our experiments was insufficient to induce ionization of the 3a1 state in liquid water, analogous to the absence of observable ionization signals for the 3a1 state using extreme ultraviolet (EUV[7]) irradiation. The area obtained by integrating the ionizing signal of liquid water $1b_1$ can equivalently represents the multiphoton absorption cross section. By fitting the relationship between δ and E according to equation 4, as shown in Fig. S6, the $^1b_1$ signal showed almost linear laser power dependence. The slope of the straight line is ~2.4, indicative of a preferred three-photon ionization scheme. Note that the three-photon ionization scheme is relevant to the ionization signal of liquid water $1b_1$, however, it might be referred to the two ionization channels ($^1\pi\pi^* \rightarrow D_0$ (π^{-1}) and $^1n\pi^* \rightarrow D_1$ (n^{-1})). The expected PKE range in a three-photon ionization scheme for these two ionization channels are also consistent with our observed PKE range.

S4. Detailed comparison with different Gaussian component fits

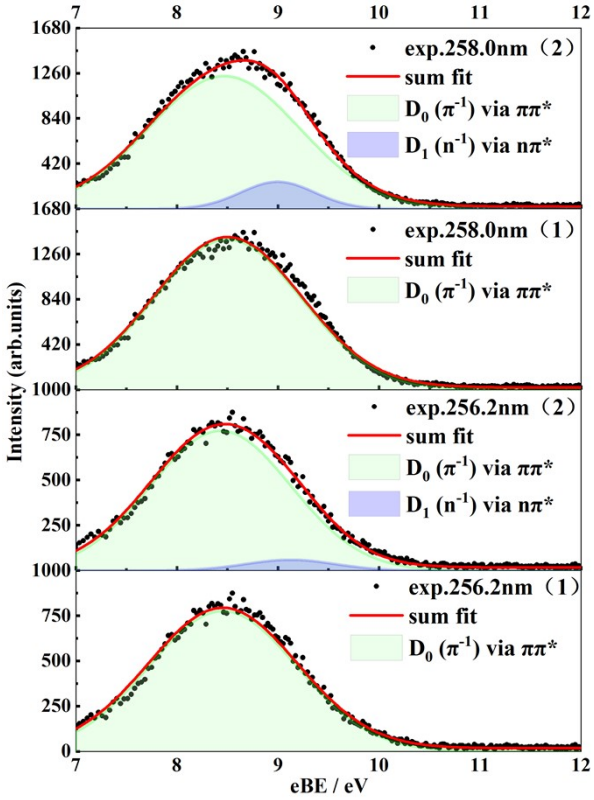

Fig. S7. Detailed comparison with one- and two-Gaussian component fits of the eBE spectra at 256.2 nm and 258.0 nm.

As discussed in the manuscript, the spectral line shape changes with ionization wavelength and laser energy. As seen from Fig. 4. in the manuscript, at 266.7 nm, the eBE spectrum can be well fitted by two Gaussian functions with a strong $^1\pi\pi^* \rightarrow D_0$ (π^{-1}) component centered at ~8.5 eV and a smaller $^1n\pi^* \rightarrow D_1$ (n^{-1}) component centered at ~9.5 eV. This feature is also obviously identifiable by eyes at 260.5, 254.8, 246.3 and 243.2 nm, but not clear at 258.0, 256.2 nm. A detailed comparison between the two-Gaussian and one-Gaussian fits at 258.0 and 256.2 nm is performed in Fig. S7. At first glance, the spectral line shapes at 256.2 nm and 258.0 nm both approximate a Gaussian shape, however, the one-Gaussian fit cannot give the best acceptable fit since it is obvious that there is a slight deviation between 9.2 and 9.5 eV. This deviation is larger for 258.0 nm than that for 256.2 nm. Instead, the two-Gaussian model can give the best acceptable fit. In contrast, although it is not shown here, the one-Gaussian model gives the best acceptable fit at 240 nm, revealing only the $^1\pi\pi^* \rightarrow D_0$ (π^{-1}) component centered at ~8.5 eV. When the laser energy is increased to more than 550 nJ, the $^1n\pi^* \rightarrow D_1$ (n^{-1}) component centered at ~9.5 eV still disappears at 240 nm.

During our fitting, Gaussian functions are primarily chosen. This is because that the instrument response usually

features a Gaussian-shaped profile especially when Gaussian-shaped laser pulses are used. Therefore, Gaussian functions are commonly utilized as a standard approach in spectral fitting, which can effectively extract crucial spectral features, including the center position, width, and intensity. However, spectral data is often subject to various broadening effects. To address and test this, we have also introduced the Voigt profile to provide a more comprehensive description of spectral characteristics. The Voigt profile combines the advantages of Gaussian and Lorentzian line shapes, offering enhanced applicability to feature the potential broadening effects. The Gaussian and Voigt functions that we used are shown in the following equations,

Gaussian:

$$I(x) = I_0 e^{-\frac{x - x_0}{2\sigma^2}} \qquad (5)$$

Lorentzian:

$$I(x) = \frac{I_0 \quad \Gamma}{\pi (x - x_0)^2 - \Gamma^2} \qquad (6)$$

Voigt:

$$I(x) = \int_{-\infty}^{\infty} G(x - y) L(y) dy \qquad (7)$$

In the context of spectroscopy, $I(x)$ represents the spectral intensity, I_0 denotes the maximum intensity, x_0 indicates the peak position, σ stands for the standard deviation of the Gaussian line shape that determines line width, Γ signifies the half-width at half-maximum of Lorentzian which also influences line width. Additionally, $G(x)$ and $L(y)$ represent Gaussian and Lorentzian line shapes respectively.

The comparative spectral fitting results for the experimental data shown in Figure 3 in the manuscript are concluded in Table S1. From a close comparation of the ^{1}nπ^*quantum yields shown in Table S1 that obtained by the two different profiles with the Gaussian and Voigt functions, we conclude that the fitting results for the ^{1}nπ^*quantum yields are in good agreement with each other. The relative changes are within an acceptable range, as seen from Table S1. A comparative fitting figure clearly exhibit this acceptable consistence, as shown in Fig S8 for the experimental wavelength of 266.7 nm. Therefore, we note that the fitting function profile with a Gaussian or Voigt function might affect the spectral fitting results for the ^{1}nπ^*quantum yields but to an acceptable extent.

Table S1. The comparative spectral fitting results for the experimental data shown in Figure 3 in the manuscript by Gaussian and Voigt functions.

Wavelength/nm	Gaussian			Voigt		
	D_0 (π^{-1})/eV	D_1 (n^{-1}) /eV	YQ(^{1}nπ^*)	D_0 (π^{-1}) /eV	D_1 (n^{-1}) /eV	YQ(^{1}nπ^*)
266.7	8.48	9.22	0.27±0.01	8.48	9.25	0.25±0.10
260.5	8.41	9.16	0.11±0.02	8.36	9.06	0.24±0.14
258.0	8.47	9.00	0.08±0.01	8.34	9.09	0.18±0.08
256.2	8.43	9.12	0.02±0.02	8.43	8.93	0.05±0.03
254.8	8.59	9.37	0.08±0.02	8.61	9.38	0.06±0.03
246.3	8.57	9.51	0.13±0.02	8.58	9.51	0.13±0.04
243.2	8.35	9.17	0.17±0.02	8.28	9.16	0.22±0.08
240.0	8.47	--	--	8.47	--	--

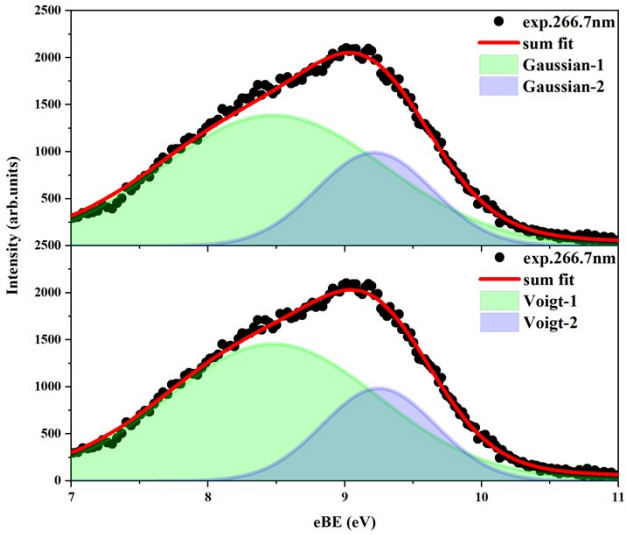

Fig. S8. A comparative fitting of the spectra obtained at 266.7nm by Gaussian and Voigt functions

S5. Wavelength-dependent vertical ionization energies

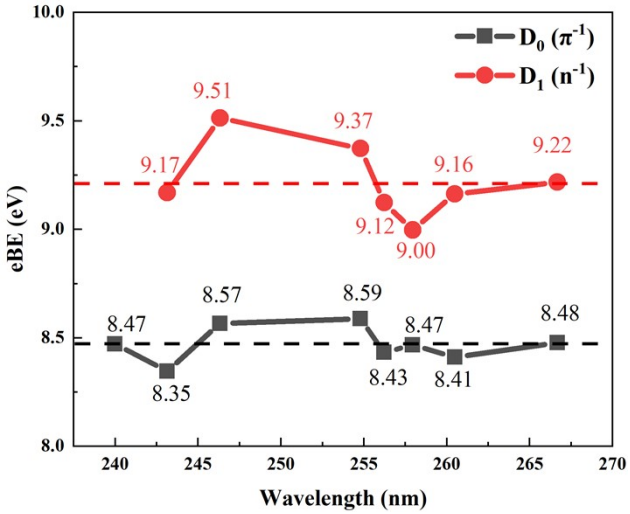

Fig. S9. Wavelength-dependent vertical ionization energies (VIEs) of D_0 and D_1 of aqueous thymidine. As indicated by the dash dot line, the averaged VIEs of D_0 and D_1 of aqueous thymidine are experimentally determined to be 8.47 ± 0.12 eV and 9.22 ± 0.29 eV, respectively.

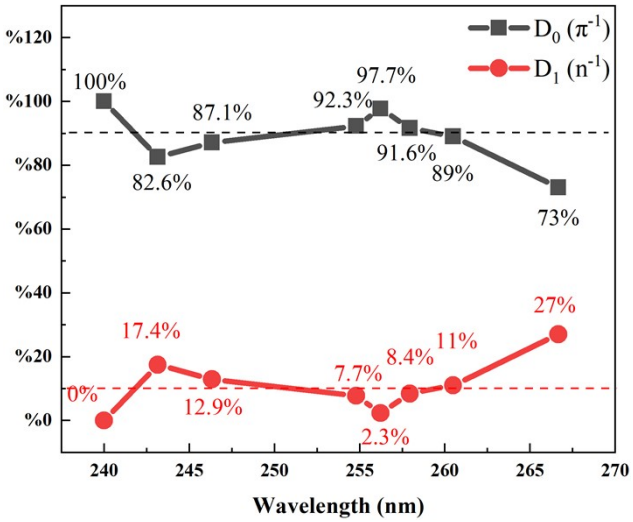

Fig. S10. The relative intensity ratios of I[^{1}nπ*] and [I[^{1}ππ*] at different ionization wavelengths. The averaged intensity ratio was 85.8% for I[^{1}ππ*] and the 14.2% for I[^{1}nπ*].

As discussed in the manuscript, we assign the eBE component centered at ~8.5 eV to the cationic ground state D_0 (π^{-1}) and the eBE component centered at ~9.5 eV to the cationic first excited state D_1 (n^{-1}), which correspond to the two resonant ionization channels from ^{1}ππ*→D_0 (π^{-1}) and ^{1}nπ*→D_1 (n^{-1}), respectively. The ionization propensity rule allows us to use the vibrational Frank-Condon envelope to identify resonant (1+2) ionization from ^{1}ππ* or ^{1}nπ*, resulting in an energy-shifted eBE vibrational envelope. In fact, the two observed eBE components are indeed found to shift around ~8.5 eV and ~9.5 eV with different ionization wavelengths, reflecting the actual wavelength resonance with the vibrionic structure of the ^{1}ππ* or ^{1}nπ* upon the first photon absorption. All the line shapes at different wavelengths can be well fitted as a superposition of two Gaussian functions with a more intense eBE component centered at ~8.5 eV and a smaller eBE component centered at ~9.5 eV, as indicated by the two color-filled Gaussian components in Fig. 3 in the manuscript. As shown in Fig. S9, the vertical ionization energies (VIEs) of D_0 and D_1 are plotted as ionization wavelengths. As an average, the averaged VIEs of D_0 and D_1 of aqueous thymidine are experimentally determined to be 8.47 ± 0.12 eV and 9.22 ± 0.29 eV, respectively. The corresponding integrated area intensity ratios of I[^{1}nπ*]/(I[^{1}nπ*]+I[^{1}ππ*]) and I[^{1}ππ*]/(I[^{1}nπ*]+I[^{1}ππ*]) (i.e., relative intensity ratios of I[^{1}nπ*] and [I[^{1}ππ*]) at different ionization wavelengths is also plotted as ionization wavelengths, as shown in Fig. S10. The averaged intensity ratio was 85.8% for I[^{1}ππ*] and the 14.2% for I[^{1}nπ*], indicating that the ^{1}nπ*→D_1 (n^{-1}) ionization channel is the minor component. As a result, the quantum yield can be obtained from the integrated area intensity ratio of I[^{1}nπ*]/(I[^{1}nπ*]+I[^{1}ππ*]).

S6. Computational methods and results

Nowadays, the quantum mechanics/molecular mechanics (QM/MM)-molecular dynamics (MD) simulation (i.e., QM/MM-MD), has been widely used to calculate both the ground and excited states of a molecule solvated in water[8-11][10-13]. Currently, this state-of-the-art QM/MM-MD is not accessible in our group. Moreover, the continuum solvation models, such as the polarizable continuum model (PCM) or the nonequilibrium polarizable continuum model (NEQ PCM), cannot take into account the specific solute−solvent interactions like hydrogen bonds and were found to give a big deviation to the experimental results when we calculated the aqueous Thd. An alternative approach is based on the cluster model of Thd+nH_2O. This method has an appropriate computational cost and has the advantage of the inclusion of specific solute−solvent interactions. The cluster model has also been widely used in aqueous system[13,14].

We use the cluster model of Thd+nH_2O to the structures and energies of the ground, excited and cationic states. Gaussian software[15] and molclus program[16] were mainly used. Firstly, we examined the effect of microhydration of water (i.e., number of waters) on the energies of the ground-state Thd+nH_2O by adding a conformational searching. The microhydration was presented for one to nine water molecules, and it was found that the lowest single point energies vary with the number of water molecules until these are almost close to each other in the complex containing six water molecules. The computational cost of Thd+nH_2O increases rapidly with the number of waters. Therefore, we chose the simple cluster model of Thd+6H_2O to perform all the calculations.

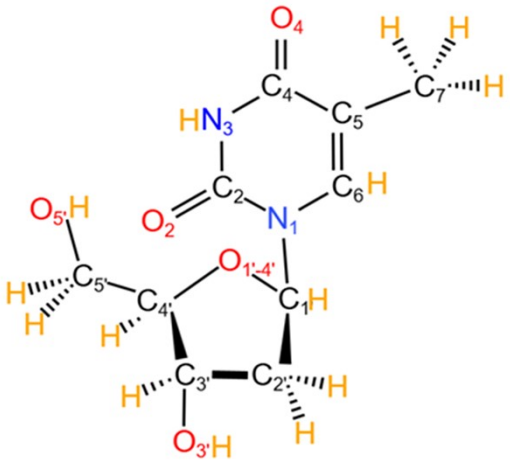

Fig. S11. Molecular structure of Thd and the numbering of its atoms.

Consistent with previous work[7,11], the molecular structure of Thd and the numbering of its atoms is shown in Fig. S11. The optimized ground-state structures of the Thd with six water molecules at the B3LYP/6-311G (d, p) level are presented in Fig. S12. Two conformations are mainly identified, similar to the previous work[17,18]. These two conformations are mainly due to the different directions between the thymine (Thy) and deoxyribonucleic acid rings, which causes some twisting around the bonds connecting the two rings. The $O_{5'}$-H bond points toward O_2 (syn-conformation, see Fig. S10. for atomic nomenclature), while the $O_{5'}$-H bond points away from O_2 (anti-conformation). The syn-conformation (shown in Fig. S12(a)) is the main one among the two conformations, and a cage-like structure is formed by water molecules and Thd molecules, as shown in Fig. S12(a). The proportions of the two conformations are 99.79% (syn-conformation, shown in Fig. S12(a)) and 0.21% (anti-conformation, shown in Fig. S12(b)), respectively, which is consistent with the conclusion of Erickson[17] and Pepino[18] et al. For different conformations, there are significant changes in the distribution of water molecules for the overall cluster structure, mainly influenced by the hydrogen bonding between $O_{5'}$-H groups.

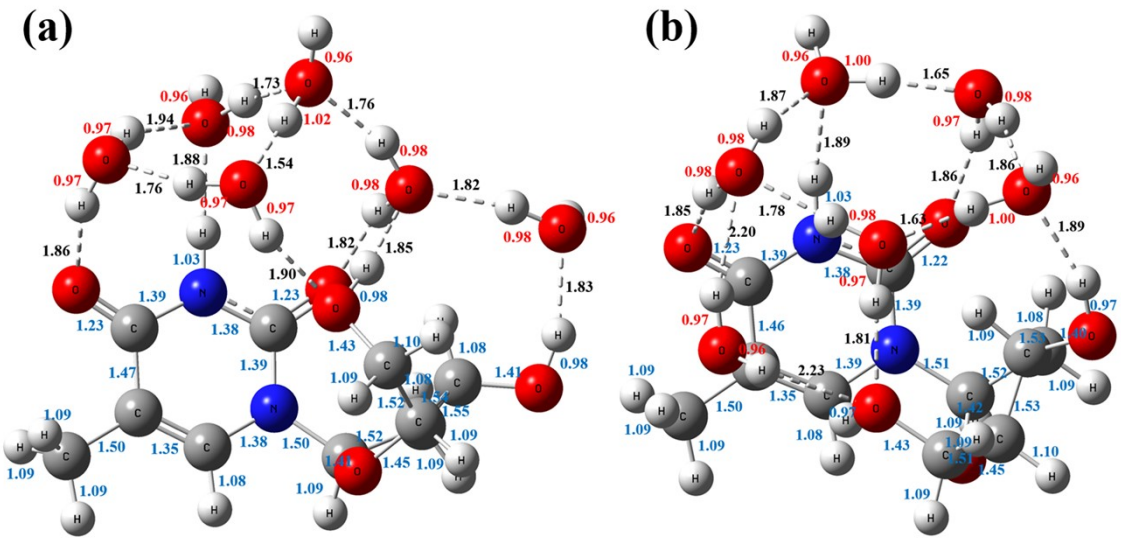

Fig. S12. The optimized ground-state structures of the Thd with six water molecules (Thd +6H_2O) at the B3LYP/6-311G (d, p) level. In the structure of Thd +6H_2O, water molecules are bound to Thy and ribose moieties, comprising two conformations that account to 99.79% (syn-conformation, shown in Fig. S12(a)) and 0.21% (anti-conformation, shown in Fig. S12(b)). Bond lengths are given in units of Å. The values for the distances between the oxygen and hydrogen atoms (black), the bond lengths of water (red), and the corresponding bond lengths of Thd (blue) are indicated.

Table S2. Calculated VEE and VIE values for the excited states of $S_1(^1n\pi^*)$ and $S_2(^1\pi\pi^*)$ and cationic states of $D_0(\pi^{-1})$ and $D_1(n^{-1})$ in a cluster model of Thd+6H_2O at different computational levels.

Model	Method/ basis sets	S_1(VEE) /eV	S_2(VEE) /eV	D_0(VIE) /eV	D_1(VIE) /eV
PCM	B3LYP /6-311G (d, p)	4.74	4.85	6.42	7.24
cluster+6H_2O	B3LYP /6-311G (d, p)	4.85	4.96	8.40	8.50

At the ground-state syn-conformation geometry, we optimized the stable structures of the first, second excited states of Thd+6H_2O at the B3LYP/6-311G (d, p) level. The single point energies were calculated, and frequencies were also performed and checked to ensure that a minimum on the potential energy surface was reached. The first excited state is $^1n\pi^*$, and the second excited state is $^1\pi\pi^*$. The $^1n\pi^*$ state is lower in energy than the $^1\pi\pi^*$ state, consistent with previous work[17]. As a result, the adiabatic excitation energies (AEEs) for the $^1\pi\pi^*$ and $^1n\pi^*$ states from the ground state can be obtained. Likewise, at the ground-state syn-conformation geometry, we optimized the stable structures of the cationic ground and first excited states of Thd+6H_2O at the B3LYP/6-311G (d, p) level. The cationic ground and first excited states are found to be D_0 (π^{-1}) and D_1 (n^{-1}), respectively. The corresponding adiabatic ionization energies (AIEs) for the $^1\pi\pi^*$ and $^1n\pi^*$ states from the ground state can be obtained.

At the ground-state syn-conformation geometry, we calculated the vertical excitation energies (VEEs) for the $^1\pi\pi^*$ and $^1n\pi^*$ states from the ground state. Likewise, we calculated the vertical ionization energies (VIEs) for the D_0 (π^{-1}) and D_1 (n^{-1}) states from the ground state. The corresponding VEEs and VIEs are summarized in Table S2. The oscillator intensities for the $^1\pi\pi^*$ and $^1n\pi^*$ states from the ground state were calculated to be $f_1(^1n\pi^*)=0.0059$ and $f_2(^1\pi\pi^*)=0.1597$, indicating the $^1n\pi^*$ state is nearly dark. We found that the VIE for the D_1 (n^{-1}) state exhibits a big deviation to the experimental value. As has already been pointed out by many work[7,13,17,19], consideration of dynamic electron correlation is important for accurate estimation of the energies and energy barriers for nuclear wave-packet motion in the excited states. This does not affect our experimental assignment of the D_1 (n^{-1}) state when we compared to the corresponding experimental vertical eBEs D_0=8.3[19], ~8.5 eV[7], D_1=~9.7[19], ~9.8[7] eV known or estimated from previous experimental work[7,19].

Table S3. Calculated Dyson norms from the different transitions at the CASSCF level in CASSCF (10,8)/cc-pVDZ and CASSCF (9,8)/cc-pVDZ.

Cluster model	Transitions	Dyson norms
Thd+6H_2O	$S_1(^1n\pi^*)\rightarrow D_0(\pi^{-1})$	0.0087
	$S_1(^1n\pi^*)\rightarrow D_1(n^{-1})$	0.6555
	$S_2(^1\pi\pi^*)\rightarrow D_0(\pi^{-1})$	0.6430
	$S_2(^1\pi\pi^*)\rightarrow D_1(n^{-1})$	0.2797

We calculated the Dyson norms[7,14] to examine Koopmans' ionization correlations for a cluster model[14] of Thd with six water molecules by the quantum chemistry software BAGEL[20]. Based on the FC structure obtained from DFT calculations, we calculate the Dyson orbitals at the CASSCF level in CASSCF (10,8)/cc-pVDZ and CASSCF (9,8)/cc-pVDZ. As listed in Table S3, the Dyson norms for the $^1\pi\pi^*$ to π^{-1} state and the $^1n\pi^*$ to n^{-1} state are large and nearly equal, suggesting that the $^1\pi\pi^*$ preferentially ionizes into D_0 (π^{-1}), whereas $^1n\pi^*$ preferentially ionizes into D_1 (n^{-1}).

References

1 J. Y. Long, Z. H. Qiu, J. Wei, D. D. Li, X. L. Song, B. Jin, B. Zhang, Liquid-Microjet Photoelectron Imaging Spectrometry for Liquid Aqueous Solutions. *Rev. Sci. Instrum.*, 2021, ***92*,** 065108.

2 Z. H. Qiu, J. Wei, D. D. Li, J. Y. Long, S. Zhang, B. Zhang, Non-adiabatic dynamics of Rydberg-excited diethylamine, *Spectrochim. Acta. A*, 2022, **274**, 121065.

3 G. K. Jarvis, M. Evans, C. Y. Ng, K. Mitsuke, Rotational-Resolved Pulsed Field Ionization Photoelectron Study of NO+ ($X^1\Sigma^+$, v^+=0–32) in the Energy Range of 9.24–16.80 eV. *J. Chem. Phys.*, 1999, **111,** 3058-3069.

4 F. Buchner, A. Lübcke, N. Heine, T. Schultz, Time-resolved photoelectron spectroscopy of liquids. *Rev. Sci. Instrum.,* 2010, **81,** 113107.

5 N. Kurahashi, S. Karashima, Y. Tang, T. Horio, B. Abulimiti, Y.-I. Suzuki, Y. Ogi, M. Oura, T. Suzuki, Photoelectron Spectroscopy of Aqueous Solutions: Streaming Potentials of NaX (X = Cl, Br, and I) Solutions and Electron Binding Energies of Liquid Water and X^-. *J. Chem. Phys.*, 2014, **140,** 174506.

6 P. M. Hare, C. E. Crespo-Hernández, B. Kohler, Solvent-Dependent Photophysics of 1-Cyclohexyluracil: Ultrafast Branching in the Initial Bright State Leads Nonradiatively to the Electronic Ground State and a Long-Lived $^1n\pi^*$ State. *J. Phys. Chem. B*, 2006, **110**, 18641-18650.

7 Y. Miura, Y. I. Yamamoto, S. Karashima, N. Orimo, A. Hara, K. Fukuoka, T. Ishiyama, T. Suzuki, Formation of Long-Lived Dark States during Electronic Relaxation of Pyrimidine Nucleobases Studied Using Extreme Ultraviolet Time-Resolved Photoelectron Spectroscopy. *J. Am. Chem. Soc.*, 2023, **145,** 3369-3381.

8 W. J. Schreier, T. E. Schrader, F. O. Koller, P. Gilch, C. E. Crespo-Hernández, V. N. Swaminathan, T. Carell, W. Zinth, Bern Kohler,Thymine Dimerization in DNA Is an Ultrafast Photoreaction, *Science*, 2007, 315, 625-629.

9 S. Thürmer, S. Malerz, F. Trinter, U. Hergenhahn, C. Lee, D. M. Neumark, G. Meijer, B. Winter, I. Wilkinson, Accurate Vertical Ionization Energy and Work Function Determinations of Liquid Water and Aqueous Solutions. *Chem. Sci.*, 2021, **12,** 10558-10582.

10 A. Nakayama, G. Arai, S. Yamazaki, T. Taketsugu, Solvent effects on the ultrafast nonradiative deactivation mechanisms of thymine in aqueous solution: Excited-state QM/MM molecular dynamics simulations. *J. Chem. Phys.*, 2013, **139,** 214304.

11 F. Buchner, A. Nakayama, S. Yamazaki, H. H. Ritze, A. Lubcke, Excited-State Relaxation of Hydrated Thymine and Thymidine Measured by Liquid-Jet Photoelectron Spectroscopy: Experiment and Simulation. *J. Am. Chem. Soc.* 2015, **137,** 2931-2938.

12 A. Henley, J. W. Riley, B. Wang, H. H. Fielding, An Experimental and Computational Study of the Effect of Aqueous Solution on the Multiphoton Ionisation Photoelectron Spectrum of Phenol. *Faraday Discuss.*, 2020, **221,** 202-218.

13 R. Improta, F. Santoro, L. Blancafort, Quantum Mechanical Studies on the Photophysics and the Photochemistry of Nucleic Acids and Nucleobases. *Chem. Rev.*, 2016, **116,** 3540-3593

14 J. W. Riley, B. Wang, J. L. Woodhouse, M. Assmann, G. A. Worth, H. H. Fielding, Unravelling the Role of an Aqueous Environment on the Electronic Structure and Ionization of Phenol Using Photoelectron Spectroscopy. *J. Phys. Chem. Lett.*, 2018, **9**, 678-682.

15 M. J. Frisch, G. W. Trucks, H. B. Schlegel, G. E. Scuseria, M. A. Robb, J. R. Cheeseman, G. Scalmani, V. Barone, G. A. Petersson, H. Nakatsuji, X. Li, M. Caricato, A. V. Marenich, J. Bloino, B. G. Janesko, R. Gomperts, B. Mennucci, H. P. Hratchian, J. V. Ortiz, A. F. Izmaylov, J. L. Sonnenberg, Williams, F. Ding, F. Lipparini, F. Egidi, J. Goings, B. Peng, A. Petrone, T. Henderson, D. Ranasinghe, V. G. Zakrzewski, J. Gao, N. Rega, G. Zheng, W. Liang, M. Hada, M. Ehara, K. Toyota, R. Fukuda, J. Hasegawa, M. Ishida, T. Nakajima, Y. Honda, O. Kitao, H. Nakai, T. Vreven, K. Throssell, Montgomery, Jr. J. A., J. E. Peralta, F. Ogliaro, M. J. Bearpark, J. J. Heyd, E. N. Brothers, K. N. Kudin, V. N. Staroverov, T. A. Keith, R. Kobayashi, J. Normand, K. Raghavachari, A. P. Rendell, J. C. Burant, S. S. Iyengar, J. Tomasi, M. Cossi, J. M. Millam, M. Klene, C. Adamo, R. Cammi, J. W. Ochterski, R. L. Martin, K. Morokuma, O. Farkas, J. B. Foresman, D. J. Fox, Gaussian 09 Rev. C.01, Gaussian, Inc.: Wallingford, CT, 2009.

16 T. Lu, Molclus program, Version 1.9.9.9, http://www.keinsci.com/research/molclus.html., accessed on Jan 25, 2023.

17 B. A. Erickson, Z. N. Heim, E. Pieri, E. Liu, T. J. Martinez, D. M. Neumark, Relaxation Dynamics of Hydrated Thymine, Thymidine, and Thymidine Monophosphate Probed by Liquid Jet Time-Resolved Photoelectron Spectroscopy. *J. Phys. Chem. A*, 2019, **123,** 10676-10684.

18 A. J. Pepino, J. Segarra-Martí, A. Nenov, R. Improta, M. Garavelli, Resolving Ultrafast Photoinduced Deactivations in Water-Solvated Pyrimidine Nucleosides. *J. Phys. Chem. Lett.*, 2017, **8,** 1777-1783.

19 P. Slavíček, B. Winter, M. Faubel, S. E. Bradforth, P. Jungwirth, Ionization Energies of Aqueous Nucleic Acids: Photoelectron Spectroscopy of Pyrimidine Nucleosides and ab Initio Calculations. *J. Am. Chem. Soc.*, 2009, **131,** 6460-6467

20 A. Humeniuk, M. Wohlgemuth, T. Suzuki, R. Mitrić, Time-resolved photoelectron imaging spectra from non-adiabatic molecular dynamics simulations. *J. Chem. Phys.*, 2013, **139,** 134104.